Electronic Supplementary Information

for

Efficient and selective seawater oxidation by manganese ferrite electrocatalysts obtained *via* a vapor phase strategy

Alessandro Bigiani,[a] Alberto Gasparotto,*[a] Gian Andrea Rizzi,[a] Cinzia Sada,[b] Raffaella Signorini,[a] Alessia Famengo,[c] Davide Barreca,*[d] Oleg I. Lebedev,[e] Evgeny Modin,[f] Mamour Sall,[g] and Chiara Maccato[ad]

[a] *Department of Chemical Sciences, Padova University and INSTM, 35131 Padova, Italy.*
[b] *Department of Physics and Astronomy, Padova University and INSTM, 35131 Padova, Italy*
[c] *CNR-ICMATE, 35127 Padova, Italy.*
[d] *CNR-ICMATE and INSTM, Department of Chemical Sciences, Padova University, 35131 Padova, Italy.*
[e] *Laboratoire CRISMAT, UMR 6508 Normandie Université, CNRS, ENSICAEN, UNICAEN, 14050 Caen Cedex 4, France.*
[f] *CIC nanoGUNE BRTA, 20018 Donostia, San Sebastian, Spain.*
[g] *CIMAP Normandie Université, CEA, CNRS, ENSICAEN, UNICAEN, 14000 Caen, France.*

* Corresponding authors. E-mail: alberto.gasparotto@unipd.it; davide.barreca@cnr.it.

Table of Contents

§ S-1. Experimental

§ S-1.1 Characterization

X-ray photoelectron spectroscopy (XPS) wide-scan spectra were recorded in the 0-1350 eV binding energy (BE) range using a constant pass energy of 100 eV, at 1.0 eV/step, with a dwell time of 50 ms. High-resolution spectra were collected using a pass energy of 50 eV, at 0.02 eV/step, with a 50 ms dwell time.

C1s and O1s peak fitting was carried out by XPSPEAK software (version 4.1),[1] using Gaussian-Lorentzian sum functions. Deconvolution of the Fe2p and Mn2p XPS signals was not attempted, since it poses a number of complications due to peak asymmetries, shake-up structures, and multiplet splitting phenomena, with several distinct contributions per oxidation state. Altogether, the strong energy overlap between the resulting spectral features complicate chemical state identification and prevent from a reliable peak fitting.[2-4] Nonetheless, it is worth noticing that the presently reported XPS results well support the net predominance of Fe^{3+} and Mn^{2+} in the fabricated MFO spinel films, in line with results provided by the other characterization techniques.

Work function measurements were carried out with the sample biased at −10.0 V.

The estimation of band gap (E_G) values was performed from reflection electron energy loss spectroscopy (REELS) spectra, after subtraction of the elastic peak and of Tougaard background.[5]

Root-mean-square roughness (RMS) values were obtained from 3×3 μm^2 atomic force microscopy (AFM) micrographs, after background subtraction and plane fitting.[3] AFM micrographs collected on different material regions enabled to confirm the specimen homogeneity.

For transmission electron microscopy (TEM) analyses, thin cross-sectional samples were prepared *via* a standard protocol by means of focused ion beam (FIB) technique, using a Helios 450s FIB/SEM (Thermo Fisher) instrument. Pre-thinned lamellas were lifted-out from the material, attached to a TEM grid and then thinned down to electron transparency. Final treatment was performed with FIB operating at 5 kV and low current (≈25 pA). The recorded images are displayed without the application of any filter/mask.

§ S-1.2 Electrochemical tests

Electrical contacts were applied to the target samples using a copper tape attached to an uncovered fluorine-doped tin oxide (FTO) conductive region (0.5×1 cm^2).

All potentials referenced to the reversible hydrogen electrode (RHE) were calculated through the relation:[6, 7]

$$E_{RHE}\ (V) = E_{MMO}\ (V) + 0.169 + 0.0592 \times pH \quad (S1)$$

The recorded E_{RHE} values were subjected to *iR* drop correction according to equation:[8]

$$E\ (V) = E_{RHE}\ (V) - iR_u \quad (S2)$$

where i and R_u are the current (in A) and the uncompensated cell resistance (in Ω), estimated from electrochemical impedance spectroscopy (EIS) as the lowest impedance in the Nyquist plots high-frequency region[9, 10] (see the values reported in Tables S5-S6 below).

EIS analyses were performed at a fixed potential of 1.5 V *vs*. RHE, with an amplitude of 5 mV, in the frequency range from 1 kHz to 100 kHz. The obtained Nyquist plots were fitted using a simple RC circuit model. The obtained charge transfer resistances are reported in Tables S5-S6).

The reported current densities were obtained by normalizing the registered currents to the sample geometric area [0.283±0.002) cm^2], which has a practical meaning in view of eventual technological applications for device engineering.[11, 12] In fact, BET surface area measurements for supported nanosystems/thin films like the present ones represent a critical problem, since conventional N_2, and even Kr, physisorption methods fail, due to the very low material mass in comparison to the supporting substrate. Alternatively, scratching of the deposited material from the FTO substrate results in further uncertainties undermining the reliability of the results, precluding thus similar measurements. In addition, the inherent uncertainty on literature data pertaining the specific capacitance of MFO deposits, also in consideration of their different composition and physicochemical characteristics,[13-16] prevents from a consistent estimation of the electrochemical active surface area (ECSA).

The oxygen evolution reaction overpotential (η) was evaluated as:[7, 10, 17-22]

$$\eta\ (V) = E\ (V) - 1.23 \quad (S3)$$

where 1.23 is the E° value for O_2 evolution.

The O_2 amount produced in OER tests was monitored during chronoamperometric (CA) analysis by headspace gas analysis using a NEOFOX-KIT-PROBE system composed by a FOSPOR-R premium grade fiber optic probe connected to a NeoFox-GT fluorimeter, and subsequently used to calculate the OER Faradaic efficiency (see below). Before each measurement, O_2 was removed by fluxing N_2 into the reaction medium. The O_2 probe was introduced into the electrochemical cell through a tightly sealed septum, and continuous readings of O_2 partial pressure and temperature were performed throughout each experiment.

The Faradaic efficiency (FE) for the OER process was calculated as:[17]

$$FE = [4 \times F \times n(O_2)/ (I \times t)] \times 100 \quad \text{(S4)}$$

where F indicates the Faraday constant (96485 C/mol), $n(O_2)$ are the moles of generated molecular oxygen, I is the current measured throughout CA, and t stands for the reaction time. The uncertainty on FE values was evaluated to be $\pm$ 1%.

For a relative comparison of the electrocatalytic activity of the present systems, the turnover frequency (TOF) is usually evaluated. The TOF is defined as the number of O_2 molecules released per second per active site,[23] and calculated according to the relation:[10, 21, 24-26]

$$TOF = (j \times A) / (4 \times F \times n) \quad \text{(S5)}$$

where j, A, F, and n indicate respectively the current density, the catalyst surface area, the Faraday constant (96485 C/mol), and the number of moles corresponding to the metal active sites in the target systems. The uncertainty on the estimated TOF values was estimated to be $\pm$ 0.05 s^{-1}. As a matter of fact, the reliable and accurate measurement of the number of active sites is a challenging issue,[23] and even the determination of the real surface area is a hard task (see the pertaining observations on page S4).[27] In the present case, assuming 100% Faradaic efficiency[28] and that all metal sites are active in the OER process,[19, 27] TOF values were obtained from equation (S5), using the measured j (A/cm^2) and the specimen geometric area A (see above). The number of moles n was evaluated from the average deposit mass [(0.103$\pm$0.005) mg, measured using a Mettler Toledo XS105 DualRange microbalance] and the MFO molar mass (MM, in g/mol) for the different systems:

$$n = (3 \times 0.103 \times 10^{-3}) / MM \quad \text{(S6)}$$

To assess the possible presence of hypochlorite species generated during the OER process,

iodometric titration was used.[3, 17] In this case, ClO^-, if present, oxidizes I^- species in alkaline solution according to the following reaction:

$$H_2O + ClO^-_{(aq)} + 2I^-_{(aq)} \rightarrow I_2 + Cl^-_{(aq)} + 2OH^-_{(aq)} \quad \text{(S7)}$$

The formed I_2 subsequently yields polyiodide ions, like I_3^-, that, in the presence of starch, generate the formation of a pink-violet complex,[29] the fingerprint for hypochlorite presence, with a ClO^- detection limit as low as $\approx 2\times10^{-7}$ M.[17] Conversely, if the solution is still colorless after starch introduction, the used electrocatalysts can be regarded as 100% selective towards OER.

§ S-2. Characterization

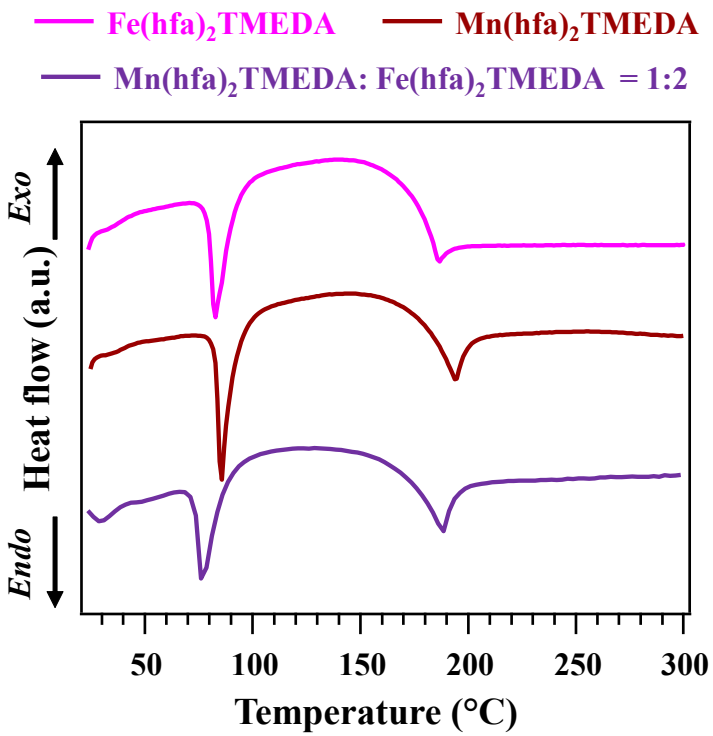

Fig. S1 Differential scanning calorimetry (DSC) curves for $Mn(hfa)_2TMEDA$, $Fe(hfa)_2TMEDA$ and their 1:2 mixture. Two endothermic peaks due to melting and vaporization are observed for the Fe (83°C, 186°C) and Mn compounds (85°C, 194°C), as well as for the Mn:Fe = 1:2 mixture (77°C, 188°C).

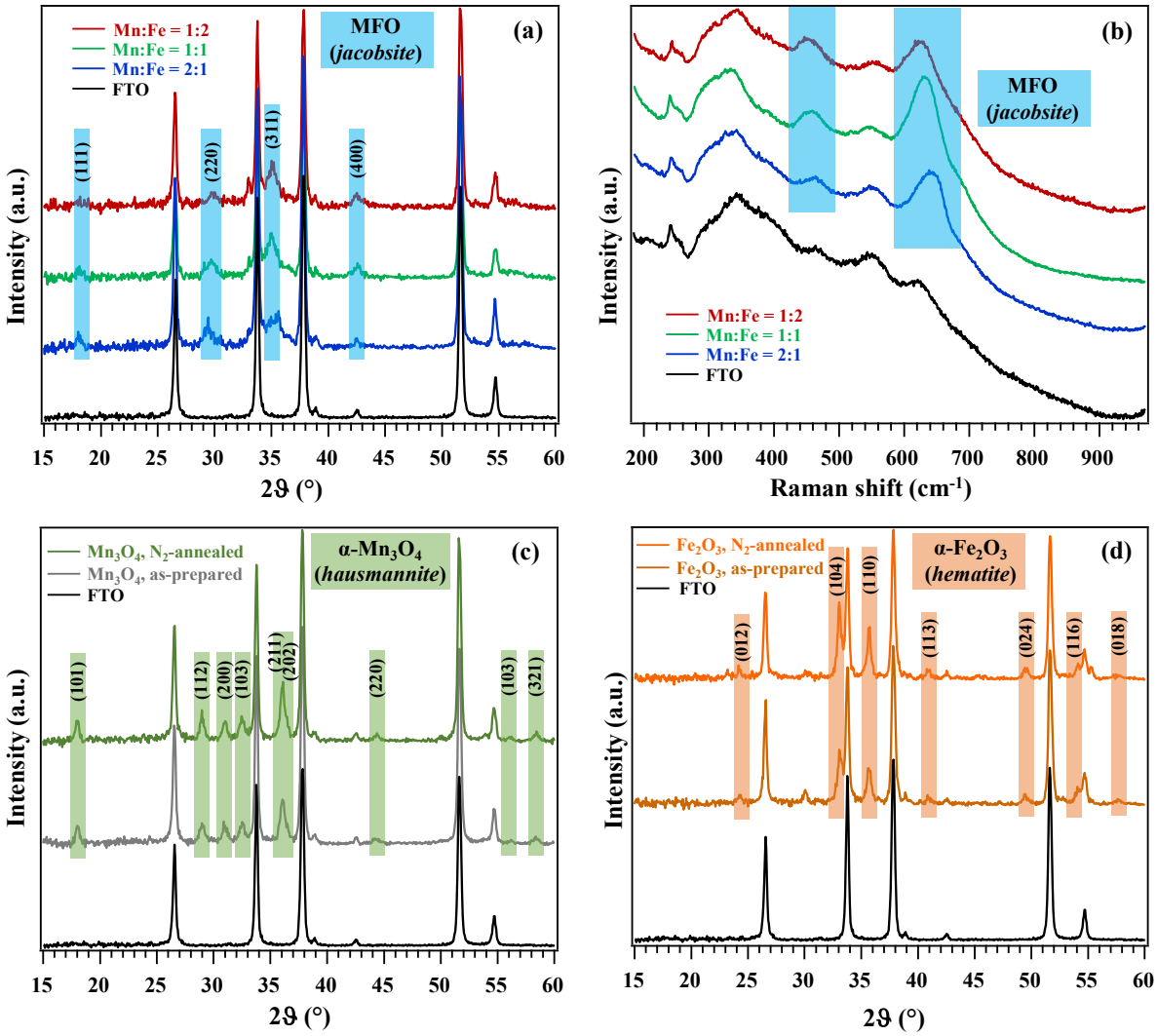

Fig. S2 XRD patterns (a) and Raman spectra (b) for as-prepared MFO films. XRD patterns of as-prepared and annealed specimens obtained by the sole vaporization of Mn (c) and Fe (d) precursors. Curves have been vertically shifted for clarity. The XRD pattern (a, c, d) and Raman spectrum (b) of bare FTO are also reported for comparison. The main signals from MFO spinel, α-Mn_3O_4, and α-Fe_2O_3 are highlighted by a pale blue, green, and orange background, respectively.

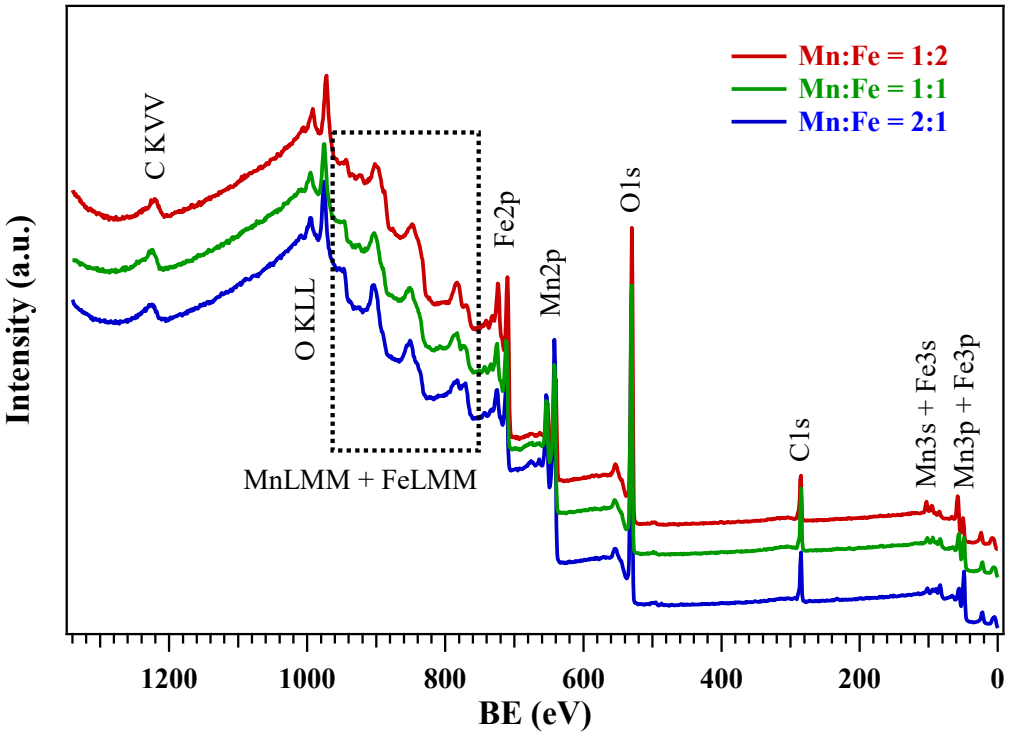

Fig. S3 XPS survey spectra for MFO deposits synthesized from different mixtures of $Mn(hfa)_2TMEDA$ and $Fe(hfa)_2TMEDA$ precursors.

	Mn (at.%)	Fe (at.%)	O (at.%)
Mn:Fe = 1:2	12.6	25.1	62.3
Mn:Fe = 1:1	18.6	17.6	63.8
Mn:Fe = 2:1	25.0	12.8	62.2

Table S1 XPS surface atomic percentages (at.%) for the target specimens calculated excluding carbon contribution.

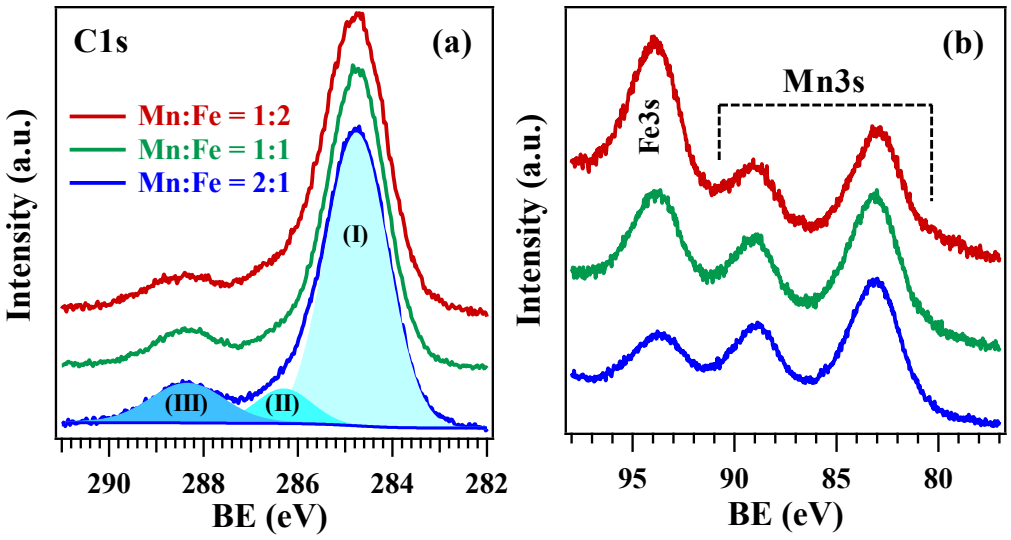

Fig. S4 C1s (a) and Mn3s (b) photoelectron peaks for MFO electrocatalysts obtained starting from different mixtures of Mn and Fe precursors.

As far as the C1s signal is concerned, the main contribution (I) was traced back to adventitious carbon (BE = 284.8 eV), whereas the two high BE components at 286.4 eV (II) and 288.4 eV (III) were attributed to C-O and C=O moieties, respectively.[30-32]

Sample	E_G (eV)	W_F (eV)	IP (eV)	EA (eV)	$\lvert E_F - VB\ (CB) \rvert$ (eV)
Mn:Fe = 1:2	1.7	4.1	5.3	3.6	1.2 (0.5)
Mn:Fe = 1:1	1.6	3.6	4.8	3.2	1.2 (0.4)
Mn:Fe = 2:1	1.4	3.7	4.8	3.4	1.1 (0.3)

Table S2 Energy gap values (E_G, estimated by REELS), work function [W_F, difference between Fermi level (E_F) and vacuum level energies], ionization potential (IP), electron affinity (EA), and absolute value of the valence (conduction) band edge separation from the Fermi level [$\lvert E_F - VB\ (CB) \rvert$] for the target specimens. IP (EA) are evaluated as the energy difference between the valence (conduction) band edges (VB and CB, respectively) and the vacuum level.[27, 33]

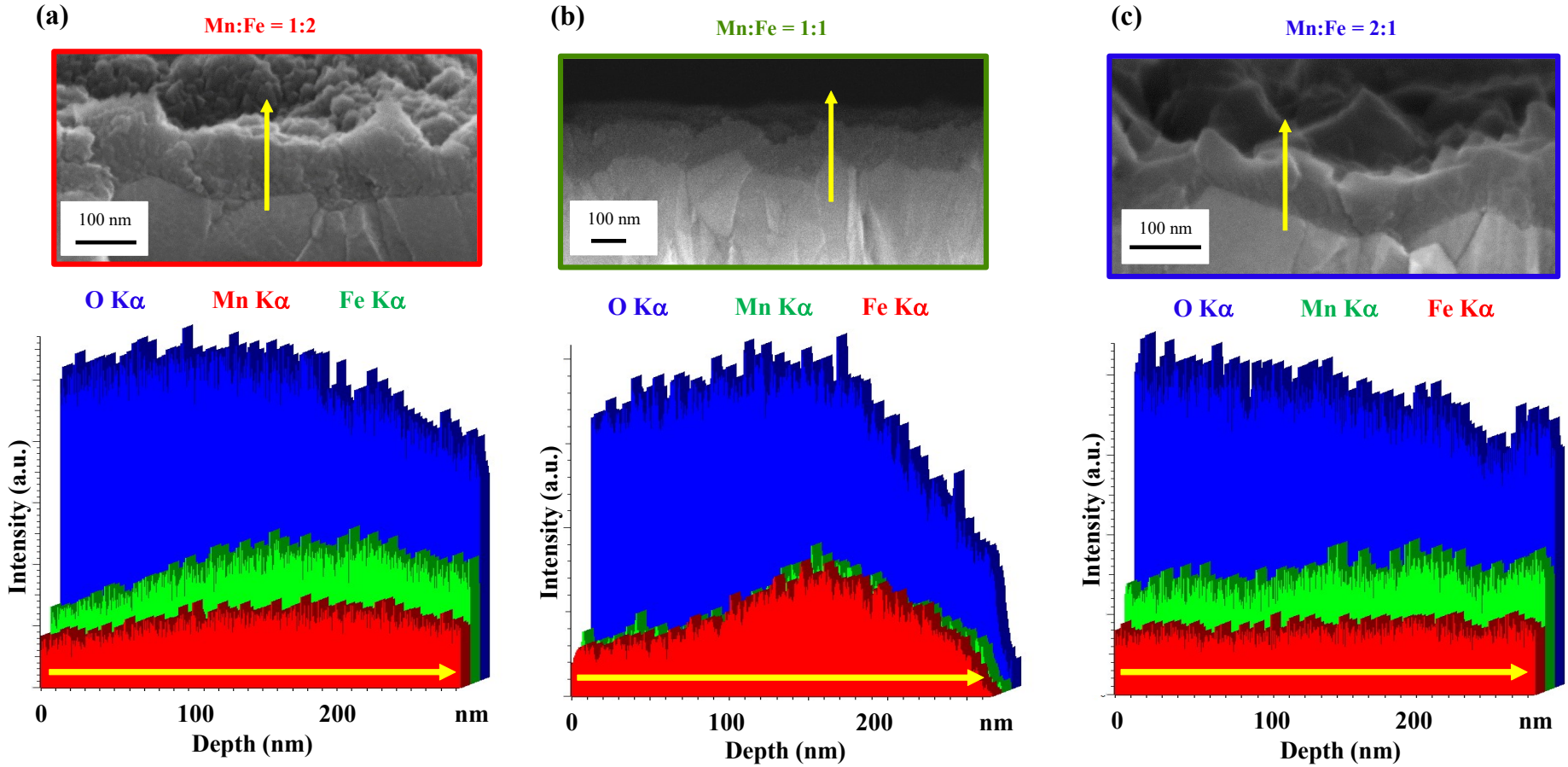

Fig. S5 Line-scan energy dispersive X-ray spectroscopy (EDXS) profiles for O, Mn, and Fe, registered on the reported cross-sectional FE-SEM images along the yellow arrows, for MFO electrocatalysts obtained from different Mn and Fe precursors mixtures: (a) Mn:Fe = 1:2; (b) Mn:Fe = 1:1; (c) Mn:Fe = 2:1.

§ S-3. Electrochemical tests and related analyses

Sample	Electrolyte	j @ 1.80 V (mA/cm^2)	Tafel slope (mV/dec)	TOF × 10^{-5} (s^{-1})	Ref.
Mn:Fe = 1:2	Simulated alkaline seawater (0.5 M KOH + 0.5 M NaCl)	(2.87±0.1)	(59±1)	1.58	Present work
Mn:Fe = 1:1		(1.89±0.1)	(63±1)	1.31	
Mn:Fe = 2:1		(1.56±0.1)	(68±1)	1.15	
Sample	**Electrolyte**	**j @ 1.80 V (mA/cm^2)**	**Tafel slope (mV/dec)**	**TOF × 10^{-5} (s^{-1})**	**Ref.**
Mn:Fe = 1:2	Adriatic alkaline seawater (pH = 13.6)	(0.28±0.1)	(64±1)	0.66	Present work
Mn:Fe = 1:1		(0.24±0.1)	(67±1)	0.50	
Mn:Fe = 2:1		(0.20±0.1)	(72±1)	0.41	

Table S3 Summary of OER activity metrics for MFO electrocatalysts in simulated alkaline seawater and Adriatic alkaline seawater splitting: current density at 1.80 V *vs*. RHE, Tafel slope values and TOF values at η = 350 mV. The onset potential at 0.02 mA/cm^2 was estimated to be very close for all the target electrocatalysts (≈1.67 V and ≈1.73 V in simulated alkaline seawater and Adriatic alkaline seawater, respectively).

Material	Electrolyte	j @ 1.80 V (mA/cm^2)	Tafel slope (mV/dec)	Ref.
Mn_2O_3 [a]	Simulated alkaline seawater (0.5 M KOH + 0.5 M NaCl)	≈12.5	67	[17]
MnO_2 [a]		≈12.4	47	[17]
MnO_2 [a]	Simulated alkaline seawater (1 M KOH + 0.5 M NaCl)	*n.a.*	131.8	[34]
α-MnO_2 [a]	Simulated alkaline seawater (0.1 M NaOH + 0.6 M NaCl)	≈0.08	81.2	[35]
β-MnO_2 [a]		≈0.033	96.7	[35]
γ-MnO_2 [a]		≈0.023	183.1	[35]
δ-MnO_2 [a]		≈0.067	186.8	[35]
Fe_2O_3 [b]	Simulated alkaline seawater (0.5 M KOH + 0.5 M NaCl)	*n.a.*	141	[3]
Fe_2O_3 [a]		≈4.5	*n.a.*	[17]
Fe_2O_3-M [b]		*n.a.*	133	[3]
Fe_2O_3-CM [b]		*n.a.*	124	[3]

Material	Electrolyte	j @ 1.80 V (mA/cm^2)	Tafel slope (mV/dec)	Ref.
Fe_2O_3-CoPi [b]	Simulated alkaline seawater (0.5 M KOH + 0.5 M NaCl)	*n.a.*	111	[3]
Fe_2O_3-M-CoPi [b]		*n.a.*	108	[3]
Fe_2O_3-CM-CoPi [b]		*n.a.*	102	[3]
Co_3O_4-Mn_2O_3 [a]		≈16.0	64	[17]
Fe_2O_3-Mn_2O_3 [a]		≈12.9	66	[17]
Co_3O_4-MnO_2 [a]		≈16.5	41	[17]
Fe_2O_3-MnO_2 [a]		≈14.5	43	[17]
MnO_2-RuO_2 [a]	Simulated alkaline seawater (1.0 M KOH + 0.5 M NaCl)	*n.a.*	75.7÷131.7	[34]
Mn_2NiO_4 [a,c]		≈75	130	[36]
$Ni_{0.85}Fe_{0.15}O$ [a]	Simulated alkaline seawater (0.1 M KOH + 2.45 wt.% NaCl)	*n.a.*	78	[37]
NiFe-LDH [a]	Simulated alkaline seawater (1.0 M KOH + 0.5 M NaCl)	*n.a.*	174	[38]

Material	Electrolyte	j @ 1.80 V (mA/cm^2)	Tafel slope (mV/dec)	Ref.
NiFe-LDH [a]	Simulated alkaline seawater (1.0 M KOH + 0.5 M NaCl)	10.0	299.4	39
NiFe-LDH [a]		*n.a.*	215÷233	40
NiAl-LDH [a]		≈110	87.9	41
NiFe-LDH/NF [a]		*n.a.*	89.2	42
MnO_x/NiFe-LDH/NF [a]		*n.a.*	72.7	42
$CaSrCo_2O_5$ [a]	Simulated alkaline seawater (0.1 M KOH + 0.5 M NaCl)	*n.a.*	107	43
$CaSrCoFeO_5$ [a]		*n.a.*	102	43
$CaSrCo_2O_5$ + FeOOH [a]		≈48	77.3	43
$La_{0.5}SrCo_{0.5}Fe_{0.5}O_x$ [a]		≈28	125	44
$CaSrCo_2O_5$ [a]		*n.a.*	107	43
$CaSrCoFeO_5$ [a]	Simulated alkaline seawater (0.1 M KOH + 0.5 M NaCl)	*n.a.*	102	43

Material	Electrolyte	j @ 1.80 V (mA/cm^2)	Tafel slope (mV/dec)	Ref.
$CaSrCo_2O_5$ + FeOOH [a]	Simulated alkaline seawater (0.1 M KOH + 0.5 M NaCl)	≈48	77.3	43
$La_{0.5}SrCo_{0.5}Fe_{0.5}O_x$ [a]		≈28	125	44
$La_{0.4}SrCo_{0.5}Fe_{0.5}O_x$ [a]		*n.a.*	86	44
$La_{0.9}Sr_{0.1}CoO_3$/NF [a]	Simulated alkaline seawater (1.0 M KOH + 3.5 wt.% NaCl)	*n.a.*	85.6	45
$La_{0.9}Sr_{0.1}CoO_3$/NF-CA [a]		*n.a.*	73.8	45
NiCoFe-PBA [a]	Simulated alkaline seawater (1.0 M KOH + 0.5 M NaCl)	*n.a.*	86.2	46
IrO_2 [a]	Simulated alkaline seawater (1.0 M KOH + 0.5 M NaCl)	*n.a.*	130	38
IrO_2 [a]	Simulated alkaline seawater (1.0 M KOH + 0.5 M NaCl)	*n.a.*	94.5	42
IrO_2 [a]	Simulated alkaline seawater (0.1 M NaOH + 0.6 M NaCl)	*n.a.*	351	35
RuO_2 [a]	Simulated alkaline seawater (1.0 M KOH + 0.5 M NaCl)	*n.a.*	81.5	34

Material	Electrolyte	j @ 1.80 V (mA/cm^2)	Tafel slope (mV/dec)	Ref.
RuO_2 [a]	Simulated alkaline seawater (1.0 M KOH + 0.5 M NaCl)	*n.a.*	73.6	47
RuO_2 [a]		*n.a.*	108.4	48
RuO_2 [a]	Simulated alkaline seawater (1.0 M KOH + 3.5 wt.% NaCl)	*n.a.*	220	49
RuO_2 [a]	Simulated alkaline seawater (1.0 M KOH + 0.6 M NaCl)	≈75	110.3	50
Mn_2O_3 [a]	Real alkaline seawater (pH: 13.5)	≈5.6	82	17
MnO_2 [a]	Real alkaline seawater (pH: 13.5)	≈6.5	72	17
Fe_2O_3-CoPi [a]	Real alkaline seawater (pH: 13.6)	*n.a.*	144	3
Fe_2O_3-M-CoPi [a]		*n.a.*	136	3
Fe_2O_3-CM-CoPi [a]		*n.a.*	125	3
Co_3O_4-Mn_2O_3 [a]		≈7.0	78	17
Fe_2O_3-Mn_2O_3 [a]	Real alkaline seawater (pH: 13.5)	≈6.7	81	17

Material	Electrolyte	j @ 1.80 V (mA/cm^2)	Tafel slope (mV/dec)	Ref.
Co_3O_4-MnO_2 [a]	Real alkaline seawater (pH: 13.5)	≈8.0	67	17
Fe_2O_3-MnO_2 [a]		≈7.0	70	17
$MnFe_2O_4$ [a]	Real alkaline seawater (1.0 M KOH)	≈100	150	51
$NiFe_2O_4$ [a]		*n.a.*	75.2	52
$CoFe_2O_4$/NF [a]		*n.a.*	67	53
$CoFe_2O_4$/NF [a]		*n.a.*	54.3	53
NiFe-LDH [a]		*n.a.*	105	51
NiCo-LDH [a]		≈280	191.8	54
NiFe-LDH/NF [a]		*n.a.*	126÷136	55
NiFe-LDH/NF [a]		*n.a.*	140.3	42
ZnFe-LDH/NF [a]		*n.a.*	94.5	56

Material	Electrolyte	j @ 1.80 V (mA/cm^2)	Tafel slope (mV/dec)	Ref.
MnO_x/NiFe-LDH/NF [a]	Real alkaline seawater (1.0 M KOH)	*n.a.*	77	42
$LaMn_{0.5}Co_{0.5}O_3$ [a]		≈138	99	57
NiCoFe-PBA [a]		*n.a.*	108.5	46
IrO_2 [a]		*n.a.*	84.3	58
RuO_2 [a]		*n.a.*	235.9	47

Table S4 OER activity metrics of previously reported electrocatalysts based on manganese or iron oxides in the splitting of simulated alkaline seawater and real alkaline seawater at room temperature. The electrochemical performances of selected RuO_2 and IrO_2 benchmarks are also reported for comparison. [a] dark conditions. [b] light conditions. [c] contains even MnO and Ni as separate phases. *n.a.* = not available. M = bulky graphic carbon nitride; CM = exfoliated graphitic carbon nitride; CoPi = cobalt(II) phosphate; LDH = layered double-hydroxide; NF = Ni foam; CA = cellulosic aerogel. Prussian blue analogues (PBAs) are a kind of perovskite-type compounds with general formula of $A_xM[Fe(CN)_6]_y \bullet mH_2O$ ($y < 1$, $0 < x < 2$), where A and M are alkali and transition metals, respectively.[46]

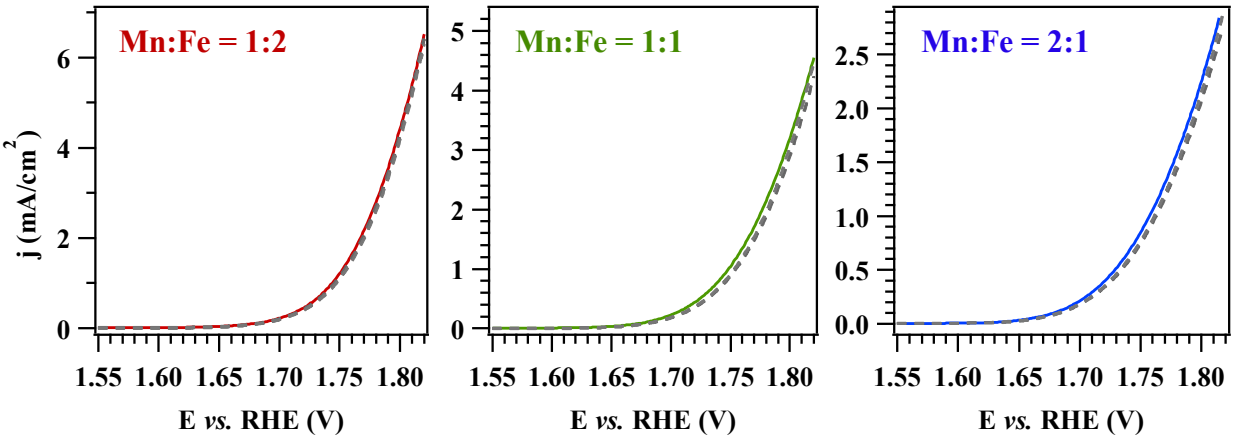

Fig. S6 Linear sweep voltammetry (LSV) curves recorded in simulated alkaline seawater (0.5 M KOH + 0.5 M NaCl) on the pristine samples (solid lines) and collected every 90 days for 6 months upon specimen storage under ambient conditions (grey dashed lines).

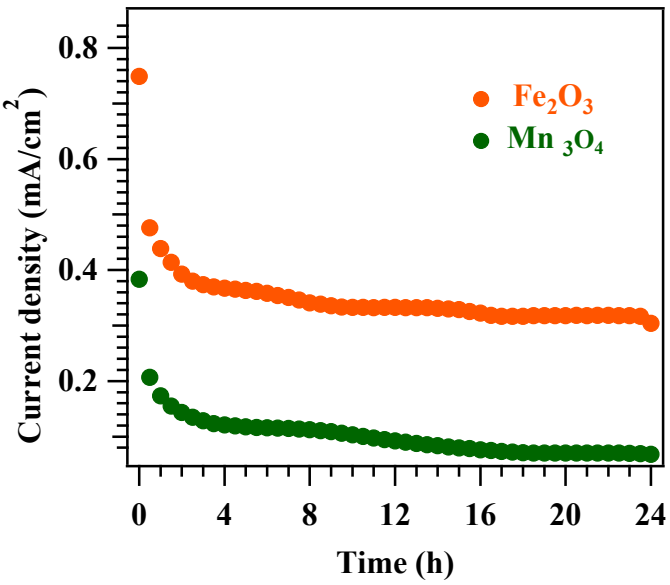

Fig. S7 Chronoamperometric tests for Mn_3O_4 and Fe_2O_3 electrocatalysts in simulated alkaline seawater, performed at 1.80 V *vs*. RHE.

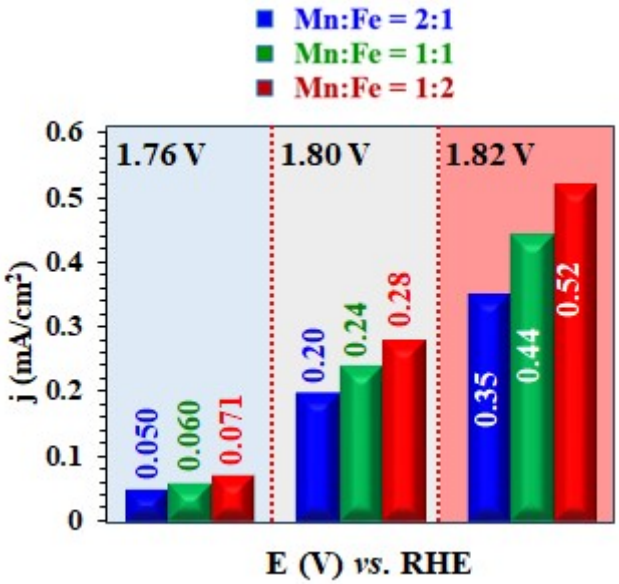

Fig. S8 Current densities at different potential values for the present electrocatalysts in Adriatic alkaline seawater.

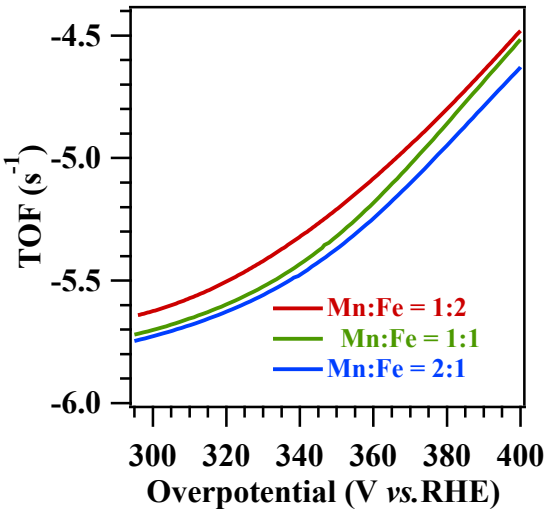

Fig. S9 TOF *vs*. overpotential plots for the present electrocatalysts in Adriatic alkaline seawater.

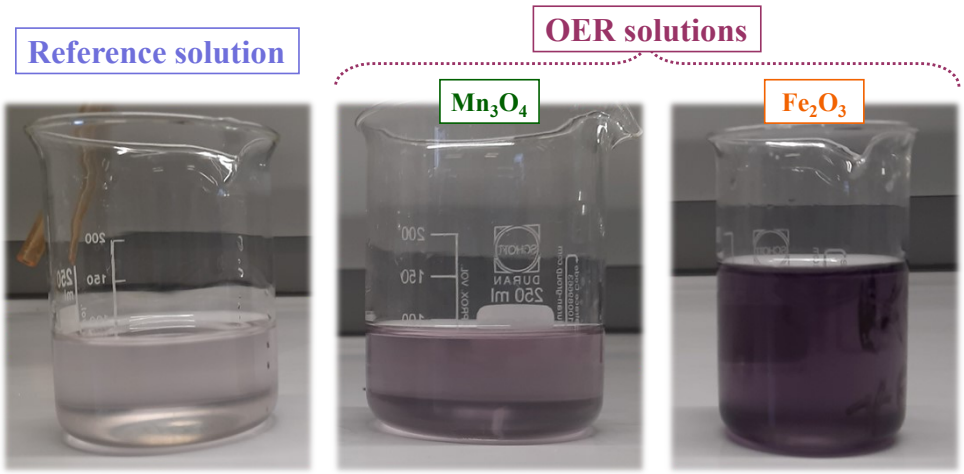

Fig. S10 Photographs of the reference and OER solutions taken upon iodometric titration for Mn_3O_4 and Fe_2O_3, evidencing ClO^- formation in both cases.

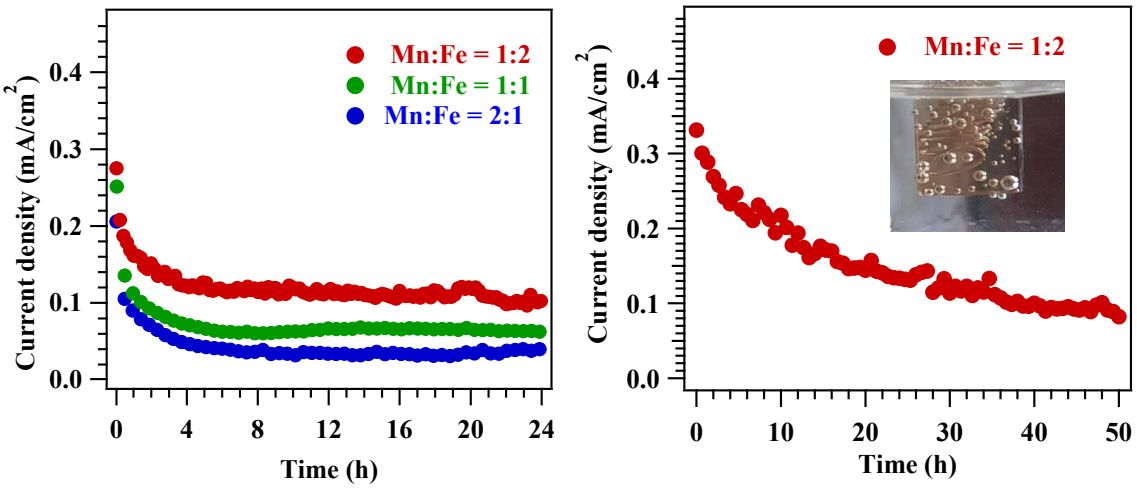

Fig. S11 Chronoamperometric tests performed on the target electrocatalysts at a fixed potential of 1.80 V *vs*. RHE in Adriatic alkaline seawater for a duration of 24 h (left panel) and of 50 h, on the best-performing Mn:Fe = 1:2 electrocatalyst (right panel). For the latter sample, the reproducibility of experimental curves revealed by the comparison of the two panels further supports the good operational stability of the developed materials. The progressive decrease of current density values as a function of time should be attributed to the evolution of O_2 bubbles on the electrode surface (see the inset in the right panel), hampering an efficient contact with the electrolyte.

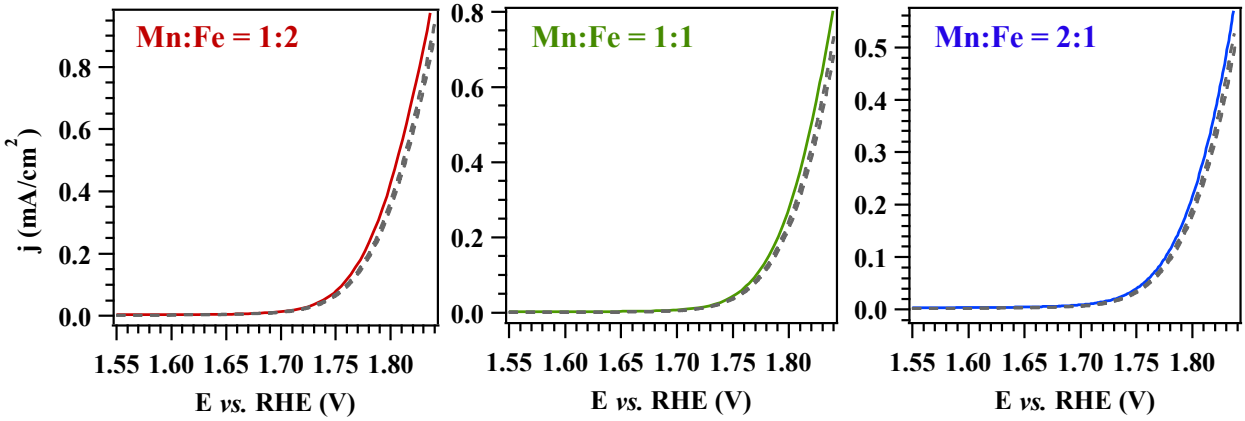

Fig. S12 LSV curves recorded in Adriatic alkaline seawater on the pristine MFO samples (solid lines) and collected every 90 days for 6 months upon specimen storage under ambient conditions (grey dashed lines).

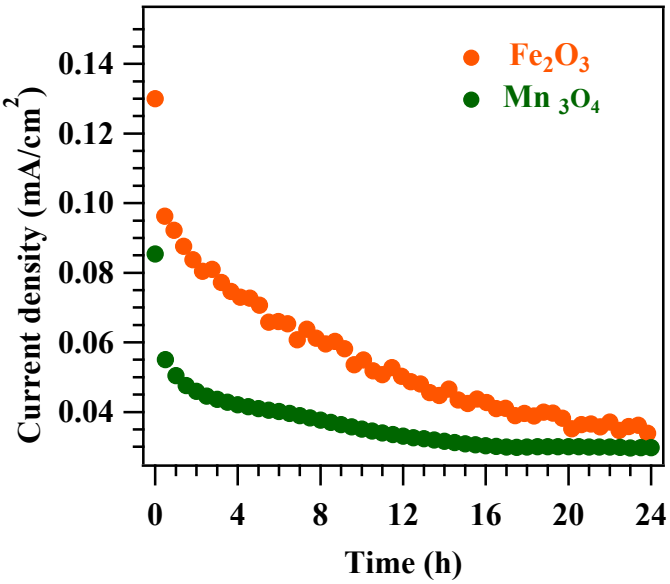

Fig. S13 Chronoamperometric tests for Mn_3O_4 and Fe_2O_3 electrocatalysts in Adriatic alkaline seawater, performed at 1.80 V *vs*. RHE.

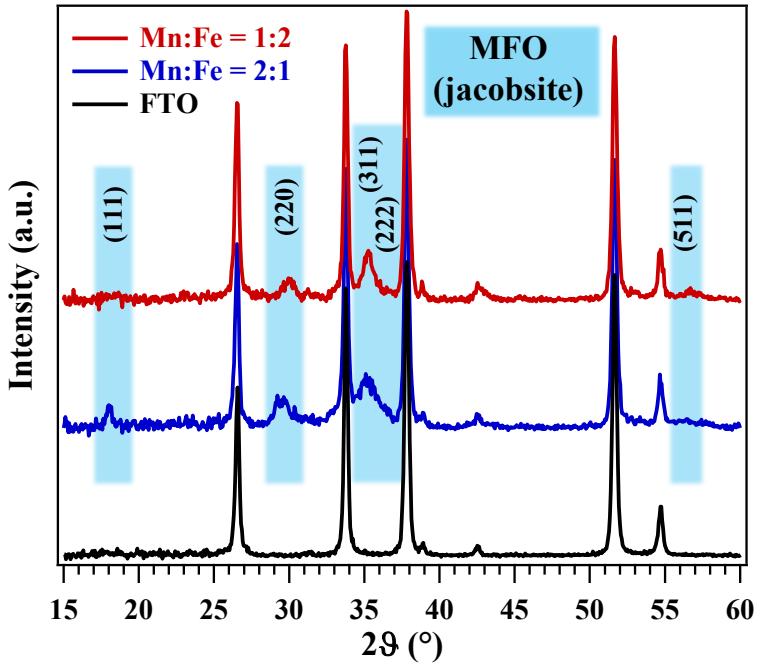

Fig. S14 XRD patterns of MFO electrocatalysts obtained from Mn:Fe = 1:2 and Mn:Fe = 2:1 precursor mixtures after completion of the tests indicated in Fig. S12. Curves have been vertically shifted for clarity. The XRD pattern of the bare FTO substrate is also reported for comparison.

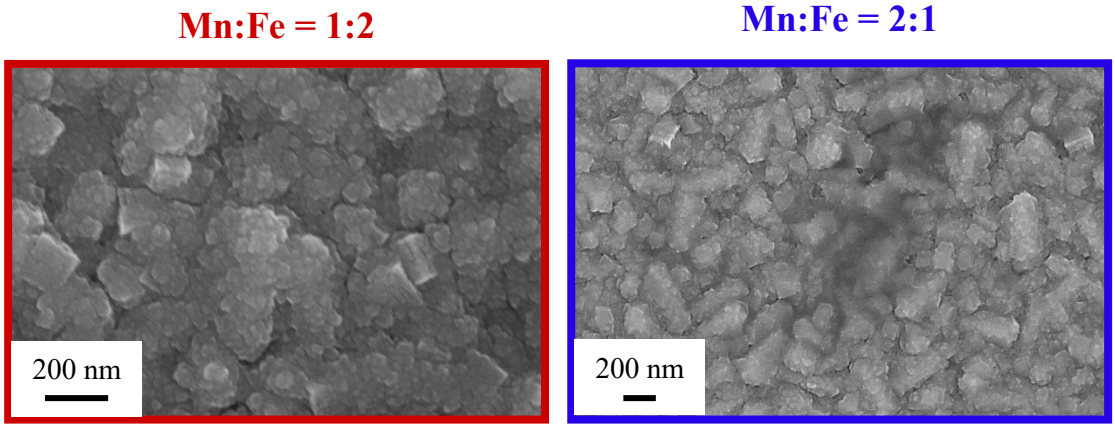

Fig. S15 Representative FE-SEM micrographs for MFO specimens synthesized from Mn:Fe = 1:2 and Mn:Fe = 2:1 precursor mixtures after completion of the tests indicated in Fig. S12.

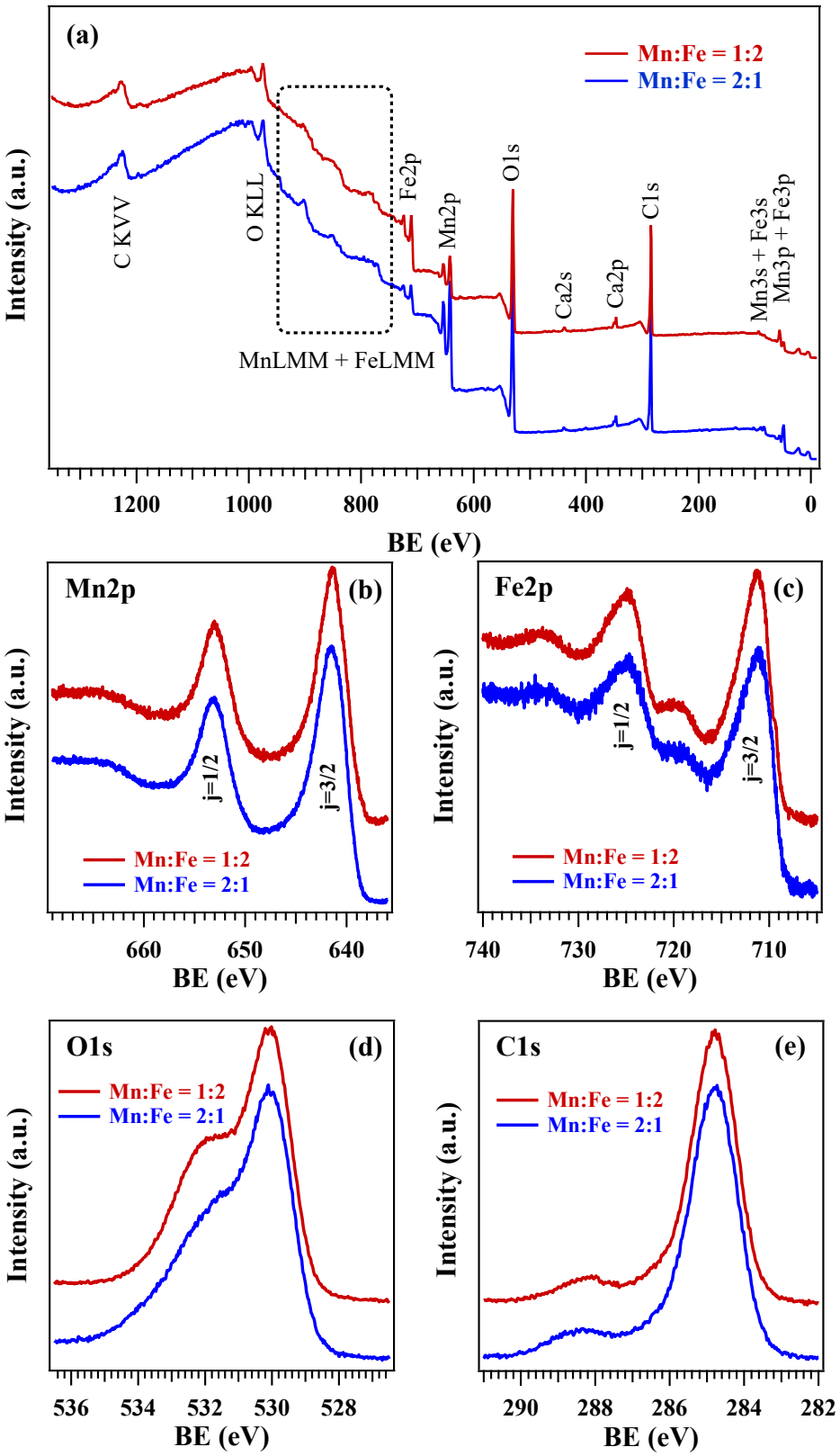

Fig. S16 XPS analysis for MFO specimens synthesized from Mn:Fe = 1:2 and Mn:Fe = 2:1 precursor mixtures after completion of the tests indicated in Fig. S12: wide-scan spectra (a), Mn2p (b), Fe2p (c), O1s (d), and C1s (e) photoelectron peaks.

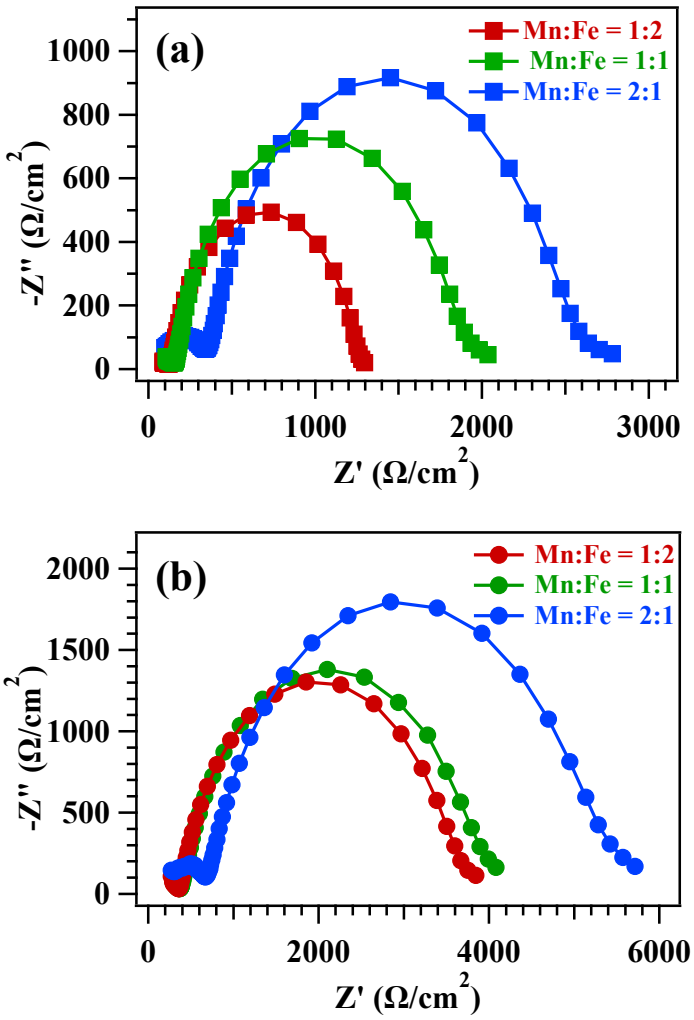

Fig. S17 EIS spectra for MFO electrocatalysts recorded in simulated alkaline seawater (a) and Adriatic alkaline seawater (b).

Sample	Electrolyte	R_u (Ω)	R_{CT} (Ω)
Mn:Fe = 1:2	Simulated alkaline seawater (0.5 M KOH + 0.5 M NaCl)	131 ± 2	1143 ± 2
Mn:Fe = 1:1		163 ± 2	1795 ± 2
Mn:Fe = 2:1		354 ± 2	2290 ± 2

Table S5 Uncompensated resistances (R_u) and charge transfer resistances (R_{CT}) for MFO electrocatalysts in simulated alkaline seawater.

Sample	Electrolyte	R_u (Ω)	R_{CT} (Ω)
Mn:Fe = 1:2	Adriatic alkaline seawater (pH = 13.6)	368± 2	3409 ± 2
Mn:Fe = 1:1		386 ± 2	3706 ± 2
Mn:Fe = 2:1		683 ± 2	4896 ± 2

Table S6 Uncompensated resistances (R_u) and charge transfer resistances (R_{CT}) for MFO electrocatalysts in Adriatic alkaline seawater.

§ S-4. References

1. https://xpspeak.software.informer.com/4.1/; Accessed October, 2025.
2. M. C. Biesinger, B. P. Payne, A. P. Grosvenor, L. W. M. Lau, A. R. Gerson and R. S. C. Smart, *Appl. Surf. Sci.*, 2011, **257**, 2717-2730.
3. M. Benedet, G. A. Rizzi, O. I. Lebedev, V. Roddatis, C. Sada, J.-L. Wree, A. Devi, C. Maccato, A. Gasparotto and D. Barreca, *J. Mater. Chem. A*, 2023, **11**, 21595-21609.
4. C. Coppi, F. Orlandi, F. Mezzadri, G. Allodi, A. Migliori, R. Cabassi, F. Cugini, M. Solzi, G. Trevisi, M. Rancan, L. Armelao, E. Gilioli and D. Delmonte, *Commun. Mater.*, 2025, **6**, 76.
5. S. Tougaard, *Surf. Interface Anal.*, 1988, **11**, 453-472.
6. M. Chen, N. Kitiphatpiboon, C. Feng, Q. Zhao, A. Abudula, Y. Ma, K. Yan and G. Guan, *Appl. Catal., B*, 2023, **330**, 122577.
7. Y. Konno, T. Yamamoto and T. Nagayama, *Nanoscale*, 2021, **13**, 12738-12749.
8. S. Anantharaj and S. Noda, *J. Mater. Chem. A*, 2022, **10**, 9348-9354.
9. T. u. Haq and Y. Haik, *ACS Sustain. Chem. Eng.*, 2022, **10**, 6622-6632.
10. S. Cosentino, M. Urso, G. Torrisi, S. Battiato, F. Priolo, A. Terrasi and S. Mirabella, *Mater. Adv.*, 2020, **1**, 1971-1979.
11. Q. Simon, D. Barreca, D. Bekermann, A. Gasparotto, C. Maccato, E. Comini, V. Gombac, P. Fornasiero, O. I. Lebedev, S. Turner, A. Devi, R. A. Fischer and G. Van Tendeloo, *Int. J. Hydrogen Energy*, 2011, **36**, 15527-15537.
12. L. Bigiani, T. Andreu, C. Maccato, E. Fois, A. Gasparotto, C. Sada, G. Tabacchi, D. Krishnan, J. Verbeeck, J. R. Morante and D. Barreca, *J. Mater. Chem. A*, 2020, **8**, 16902-16907.
13. C. C. L. McCrory, S. Jung, J. C. Peters and T. F. Jaramillo, *J. Am. Chem. Soc.*, 2013, **135**, 16977-16987.
14. P. Connor, J. Schuch, B. Kaiser and W. Jaegermann, *Z. Phys. Chem.*, 2020, **234**, 979.
15. Y. Wang, H. Arandiyan, K. Dastafkan, Y. Li and C. Zhao, *Chem. Res. Chin. Univ.*, 2020, **36**, 360-365.
16. C. Wei, S. Sun, D. Mandler, X. Wang, S. Z. Qiao and Z. J. Xu, *Chem. Soc. Rev.*, 2019, **48**, 2518-2534.

17. L. Bigiani, D. Barreca, A. Gasparotto, T. Andreu, J. Verbeeck, C. Sada, E. Modin, O. I. Lebedev, J. R. Morante and C. Maccato, *Appl. Catal., B*, 2021, **284**, 119684.
18. C. Maccato, L. Bigiani, L. Girardi, A. Gasparotto, O. I. Lebedev, E. Modin, D. Barreca and G. A. Rizzi, *Adv. Mater. Interfaces*, 2021, **8**, 2100763.
19. V. D. Silva, T. A. Simões, J. P. F. Grilo, E. S. Medeiros and D. A. Macedo, *J. Mater. Sci.*, 2020, **55**, 6648-6659.
20. N. Akechatree, K. Lakshmanan, R. Rajendran, T. Rojviroon, O. Rojviroon and S. Sirivithayapakorn, *J. Water Process Eng.*, 2025, **77**, 108590.
21. M. Umair, M. M. Hassan, B. M. Alotaibi, H. A. Alyousef, A. W. Alrowaily, A. G. Al -Sehemi and K. Tahir, *J. Sol-Gel Sci. Technol.*, 2025, **116**, 1088-1100.
22. M. Ramzan, S. Gouadria, A. G. AlShami and A. Kumar, *Inorg. Chem. Comm.*, 2025, **178**, 114530.
23. M. S. Burke, M. G. Kast, L. Trotochaud, A. M. Smith and S. W. Boettcher, *J. Am. Chem. Soc.*, 2015, **137**, 3638-3648.
24. M. Benedet, A. Gallo, C. Maccato, G. A. Rizzi, D. Barreca, O. I. Lebedev, E. Modin, R. McGlynn, D. Mariotti and A. Gasparotto, *ACS Appl. Mater. Interfaces*, 2023, **15**, 47368-47380.
25. N. Srinivasa, J. P. Hughes, P. S. Adarakatti, M. C, S. J. Rowley-Neale, A. S and C. E. Banks, *RSC Adv.*, 2021, **11**, 14654-14664.
26. M. Tang, Y. Zou, Z. Jiang, P. Ma, Z. Zhou, X. Zhu, J. Bao and S.-G. Sun, *J. Energy Chem.*, 2024, **97**, 12-19.
27. C. Maccato, D. Barreca, L. Signorin, E. Scattolin, G. Tabacchi, E. Fois, C. Sada, O. I. Lebedev, A. Gasparotto, E. Modin, E. Pierobon, N. El Habra and G. A. Rizzi, *Catal. Sci. Technol.*, 2025, **15**, 6358-6371.
28. J. Kim, P.-C. Shih, K.-C. Tsao, Y.-T. Pan, X. Yin, C.-J. Sun and H. Yang, *J. Am. Chem. Soc.*, 2017, **139**, 12076-12083.
29. J. Mendham, R. C. Denney, J. D. Barnes, M. J. K. Thomas, *Vogel's Quantitative Chemical Analysis* (6th ed.), Prentice Hall, New York, 2000.
30. Z. Cheng, S. Luo, X. Li, S. Zhang, T. Thang Nguyen, M. Guo and X. Gao, *Appl. Surf. Sci.*, 2021, **566**, 150654.

31. J. F. Moulder, W. F. Stickle, P. E. Sobol and K. D. Bomben, *Handbook of X-ray Photoelectron Spectroscopy*, Physical Electronics Division, Perkin-Elmer Corporation, 1992.
32. A. Gasparotto, C. Maccato, A. Petala, S. Bebelis, C. Sada, D. I. Kondarides and D. Barreca, *ACS Appl. Energy Mater.*, 2019, **2**, 8294-8302.
33. M. Benedet, C. Maccato, G. Pagot, C. Invernizzi, C. Sada, V. Di Noto, G. A. Rizzi, E. Fois, G. Tabacchi and D. Barreca, *J. Phys. Chem. C*, 2023, **127**, 22304-22314.
34. Y. Pi, Q. Mao, M. Jia, Z. Qiu, Y. Fan, S. Zhang and H. Pang, *Mater. Today Chem.*, 2025, **48**, 102961.
35. S. Bishwanathan and P. K. Gupta, *ACS Appl. Energy Mater.*, 2024, **7**, 5467-5478.
36. S. Barua, A. Balčiūnaitė, D. Upskuvienė, J. Vaičiūnienė, L. Tamašauskaitė-Tamašiūnaitė and E. Norkus, *Coatings*, 2024, **14**, 1074.
37. S. El Boumlasy, M. Pascale, O. De Luca, T. Caruso, S. Mirabella, A. Terrasi, A. S. Aricò and F. Ruffino, *Appl. Surf. Sci. Adv.*, 2025, **28**, 100809.
38. S. Y. Jung, J. Lee, K. Aydin, J. Jang, C. Ahn, T. Kim, H. Han and Y. K. Jeong, *Appl. Surf. Sci.*, 2024, **649**, 159097.
39. Y. Du, Y. Zhang, X. Pu, X. Fu, X. Li, L. Bai, Y. Chen and J. Qian, *Chemosphere*, 2023, **312**, 137203.
40. S. Y. Jung, S. Kang, K. M. Kim, S. Mhin, J. C. Kim, S. J. Kim, E. Enkhtuvshin, S. Choi and H. Han, *Appl. Surf. Sci.*, 2021, **568**, 150965.
41. R. Dai, J. Zeng, P. Qian, S. Zhang, S. Li, Z. M. El-Bahy, H. Hu, Y. Zhou and X. Xu, *ACS Appl. Mater. Interfaces*, 2026, **18**, 1478-1489.
42. Z. Wang, C. Wang, L. Ye, X. Liu, L. Xin, Y. Yang, L. Wang, W. Hou, Y. Wen and T. Zhan, *Inorg. Chem.*, 2022, **61**, 15256-15265.
43. X. Wang, J. Chen, L. Xu, J. Miao, J. Sunarso, X. Wang, W. Cao, Y. Yang and W. Zhou, *J. Power Sources*, 2024, **614**, 235017.
44. C. Xu, L. Xu, J. Chen, X. Wang, S. Gao, J. Miao, R. Ran and W. Zhou, *Energy Environ. Mater.*, 2026, **9**, e70117.
45. H. Zhang, X. Xu, G. Zhang, J. Yang and Y. Lu, *Colloids Surf., A*, 2024, **695**, 134027.
46. F. Ma, C. Wang, Y. An, Y. Liu, X. Xin, K. Fan, L. Wang, G. Chen, Z. Hu and T. Zhan, *Inorg.*

Chem., 2025, **64**, 11165-11176.

47. R. Liu, Q. Yang, Y. Pang, H. Li, Y. Liu, W. Wang, Z. Wang, R. Chang, X. Tian, J. Lai and L. Wang, *Small*, 2025, **21**, 2500518.
48. P.-J. Deng, Y. Liu, H. Liu, X. Li, J. Lu, S. Jing and P. Tsiakaras, *Adv. Energy Mater.*, 2024, **14**, 2400053.
49. Y. Liu, L. Chen, Y. Wang, Y. Dong, L. Zhou, S. I. Córdoba de Torresi, K. I. Ozoemena and X.-Y. Yang, *Front. Chem. Sci. Eng.*, 2023, **17**, 1698-1706.
50. L. Zhuang, J. Li, K. Wang, Z. Li, M. Zhu and Z. Xu, *Adv. Funct. Mater.*, 2022, **32**, 2201127.
51. H. Guermazi, M. Smari, A. Tahir, M. Y. Haik, T. Mnasri, T. u. Haq and Y. Haik, *Int. J. Hydrogen Energy*, 2025, **157**, 150468.
52. Y. Wu, Y. Yu, W. Shen, Y. Jiang, R. He and M. Li, *J. Colloid Interface Sci.*, 2024, **670**, 132-141.
53. F. Duan, Y. Guo, Y. Huang, G. Ke, T. Han, Y. Zhou and H. He, *Appl. Surf. Sci.*, 2025, **709**, 163795.
54. M. Zhang, Y. Sun, C. Meng, Q. Xu, Y. Zhang, X. Li, L. Fan, T. Li and Y. Li, *J. Mater. Chem. A*, 2025, **13**, 9886-9898.
55. P. K. Prabhakaran, A. K. Abidoye, S. Roy and V. V. Krishnan, *Mater. Today Sustainability*, 2025, **31**, 101130.
56. M. Vedanarayanan, C.-M. Chen and M. G. Sethuraman, *ACS Appl. Energy Mater.*, 2024, **7**, 7260-7271.
57. J. Dai, J. Xian, K. Liu, Z. Wu, M. Fan, S. Qin, H. Jiang, W. Xu, H. Jin and J. Wan, *Chin. J. Catal.*, 2025, **74**, 228-239.
58. J. Fan, X. Xiang, Y. Liu, X. Yang, N. Shi, D. Xu, C. Zhou, M. Han, J. Bao and W. Huang, *SusMat*, 2025, **5**, e70010.